Electronic Supplementary Information (ESI)

Regulating electrode/electrolyte interfacial chemistry enables 4.6 V ultra-stable fast charging of commercial $LiCoO_2$

Anping Zhang,[af] Zhihong Bi,[af] Gongrui Wang,[a] Shihao Liao,[a] Pratteek Das,[a] Hu Lin,[a] Mingrun Li,[a] Yan Yu,* [c] Xinliang Feng,* [bd] Xinhe Bao,[a] and Zhong-Shuai Wu * [ae]

[a]State Key Laboratory of Catalysis, Dalian Institute of Chemical Physics, Chinese Academy of Sciences, 457 Zhongshan Road, Dalian 116023, China. E-mail: wuzs@dicp.ac.cn

[b]Center for Advancing Electronics Dresden (cfaed), Faculty of Chemistry and Food Chemistry, Technische Universität Dresden, Dresden 01062, Germany. E-mail: xinliang.feng@tu-dresden.de

[c]Hefei National Research Center for Physical Sciences at the Microscale, Department of Materials Science and Engineering, CAS Key Laboratory of Materials for Energy Conversion, University of Science and Technology of China, Hefei 230026, Anhui, China. E-mail: yanyumse@ustc.edu.cn

[d]Max Planck Institute of Microstructure Physics, Halle (Saale) 06120, Germany

[e]Dalian National Laboratory for Clean Energy, Chinese Academy of Sciences, 457 Zhongshan Road, Dalian 116023, China

[f]University of Chinese Academy of Sciences, 19 A Yuquan Road, Shijingshan District, Beijing 100049, China

Methods

Preparation of Electrodes, Electrolytes and Cells

The commercial LCO (JOHN LONG in Beijing), Ni-rich (KJ GROUP), Co-free (Qingdao LNCM Co.,Ltd), and graphite (BTR) were purchased and used for electrodes. $LiPF_6$, EC, FEC, DFEC, DEC, FEMC, $LiPO_2F_2$, and TTE were purchased from DoDochem. Commercial electrolytes (1 M $LiPF_6$ in EC/DEC (1:1 in vol), denoted as TCE) was purchased from DoDochem. Preparations of electrolytes were all carried out in an argon-filled glove box with O_2 and H_2O contents below 0.1 ppm. Specifically, 1 M $LiPF_6$ in FEMC:DFEC:FEC:TTE was prepared and defined as FE. Different amounts of $LiPO_2F_2$ (0.005, 0.02 and 0.05 M) were added into FE to obtain FE-0.005P, FPE and FE-0.05P, respectively. The LCO, Ni-rich and Co-free electrodes were prepared using aluminum (Al) foil current collectors, coated beforehand with slurries containing cathode materials, Ketjen black (ECP600JD), and binder (poly(vinylidene fluoride)) in a weight ratio of 80:10:10. Subsequently, the obtained electrodes were dried in a vacuum oven at 100 °C for 12 h. The mass loading of active materials was ~3 mg cm^{-2} (diameter 12 mm). Lithium foil with a thickness of 450 μm was used as the anode and 40 μL electrolyte was injected and filled into the cell before it was encapsulated. The graphite electrode was prepared similarly using copper (Cu) foil current collectors, with slurries containing graphite, acetylene black, and carboxy methyl cellulose sodium (CMC) in deionized water. The N/P ratio (negative/positive capacity ratio) is controlled between 1.1 and 1.5. For stacked pouch-type graphite||LCO full cells, the LCO cathode slurry was first prepared by mixing LCO, ECP600JD and

PVDF in a weight ratio of 94:3:3, and LCO cathode was fabricated by coating the slurry onto Al foil current collector and dried at 120 °C for 24 h under vacuum. Then the graphite anode slurry was prepared by mixing graphite, acetylene black, styrene butadiene rubber (SBR) and CMC in a weight ratio of 94.5:2:2:1.5, and then the slurry was coated onto Cu foil current collector and dried at 120 °C for 24 h under vacuum. The electrolyte consumption was about ~3.5 g Ah^{-1}. The active material loading of LCO cathode was about 12 mg cm^{-2} (on both sides of the Al foil current collector). The N/P ratio was controlled ~ 1.1.

Characterization

The wettability of electrolytes was tested using a contact angle measuring instrument (DSA100). The ionic conductivity of different electrolytes was measured by a DDS-11A at room temperature. The phases and structures of the electrode materials and electrolytes were characterized by X-ray powder diffraction (XRD, SmartLab SE, Rigaku, with Cu Kα of wavelength 1.542 Å) and Raman spectra (Bruker Optics Senterra, 532 nm). The morphological and structural characterizations of samples were examined using scanning electron microscopy (SEM, Quanta 200F) and high-resolution transmission electron microscopy (HRTEM, ARM300, JEOL) at different voltages (60 kV, 200 kV) coupled with electron energy loss spectroscopy (EELS, Aztec, Oxford Instruments). The HRTEM samples were prepared through 2-30 kV Ga ion beam dual-focused ion beam electron microscopy (FIB, Helios 450HP, FEI). The surface chemistries of electrodes after cycling were detected by X-ray photoelectron spectroscopy (XPS, Thermo Scientific *K*α spectrometer) and time of flight secondary

ion mass spectrometry (TOF-SIMS, TOF.SIMS 5-100). A pulsed 30 keV Bi^{1+} (20 ns) ion beam was used for depth analysis in high current mode, and a 500 eV Cs^{+} (negative) ion beam was applied for sputtering of the samples with a sputtering area of 300 μm × 300 μm. Typical analysis area is 50 μm × 50 μm. The cycled electrodes were obtained from coin cells, and then washed 3 times with dimethyl carbonate and dried under vacuum before testing.

Electrochemical Measurements

The electrochemical performance of electrolytes was tested in 2016-type coin half cells with a polypropylene microporous film (Celgard 2500) as the separator, assembled in an argon-filled glove box with O_2 and H_2O contents below 0.1 ppm. Li||Cu half cells assembled with 16 mm diameter Cu foils and 12 mm diameter Li metal foils to study the coulombic efficiency in the corresponding electrolytes. The cycling and rate performances were tested between 3 and 4.6 V *vs.* Li^{+}/Li (0.2 C for the first three cycles, 1 C = 274 mA g^{-1}) with Wuhan Land testing systems (CT3002A). All coin half cells were activated at a rate of 0.2 C for 3 cycles and then operated for the subsequent cycles (3-4.6 V) if not specially indicated. For pouch full cells, the formation process was firstly completed: firstly charging at 0.02 C for 2 h and rested for 5 min, repeating this process twice, and then charging to 4.55 V at 0.2 C. Then, the pouch cells were discharged to 3.0 V at 0.2 C, and the second galvanostatic charge and discharge (GCD) cycle was conducted at 0.2 C at 3.0–4.55 V. The linear sweep voltammetry (LSV) was at the voltage range of 3.0 ~ 5.5 V with Li||Al (coated with Carbon ECP600JD and PVDF) configuration at a scan rate of 0.2 mV s^{-1}. The floating charge

(Chronoamperometry) test was performed on a CHI 760E electrochemical workstation by holding the LCO electrode at a constant charging voltage of 4.6 V for 10 h. Cyclic voltammetry (CV) tests were operated on a CHI 760E electrochemical workstation in the potential range of 3-4.6 V *vs.* Li^+/Li at a scan rate of 0.1 mV s^{-1}. Electrochemical impedance spectroscopy (EIS) measurements were carried out on a CHI 760E electrochemical workstation over the frequency range of 100 kHz to 0.01 Hz. Galvanostatic intermittent titration technique (GITT) curves were tested after 6 and 200 cycles by applying a pulse current of 0.2 C for 10 min with a time interval of 10 min in the voltage range of 3-4.6 V.

Density Functional Theory Calculation

The density functional theory calculations of the highest occupied molecular orbital (HOMO) and the lowest unoccupied molecular orbital (LUMO) were performed with the Gaussian 09 and Gauss View 5.0 software package with B3LYP/6-311++G (d, p) basis set level.[1, 2] The electrostatic potential (ESP) calculations were carried out using DMol3 module in Materials Studio software.[3] The geometry optimizations were performed with generalized-gradient approximation (GGA)/BLYP functional and double numerical plus d-functions (DND) basis set.[3, 4]

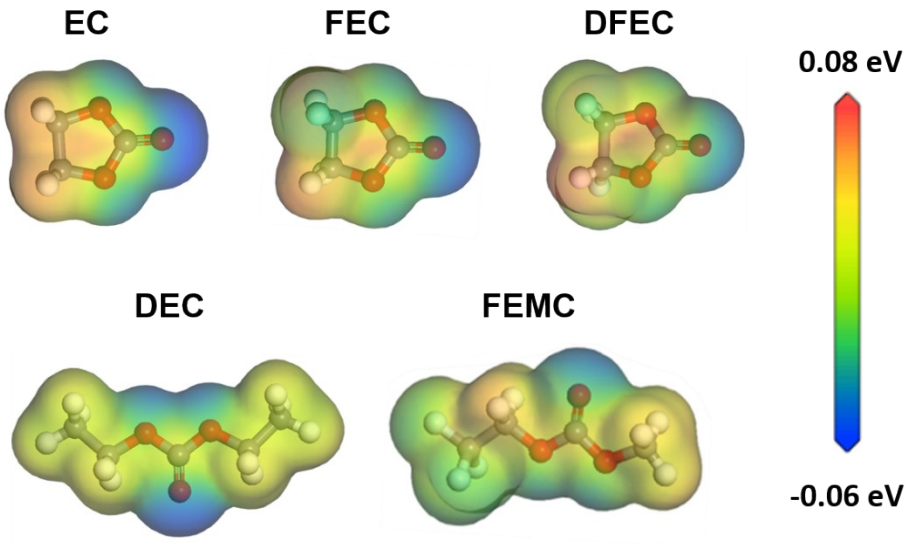

Fig. S1 Charge distributions of different solvents in the electrolytes.

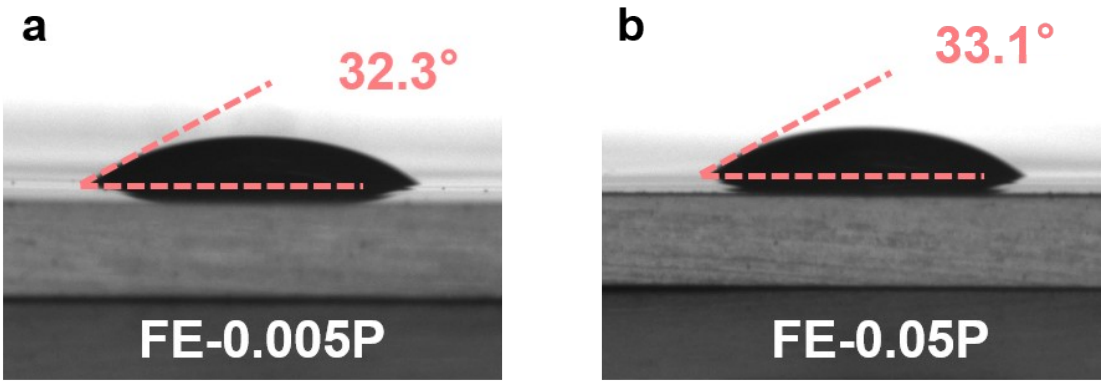

Fig. S2 Contact angles of (a) FE-0.005P and (b) FE-0.05P with the separator.

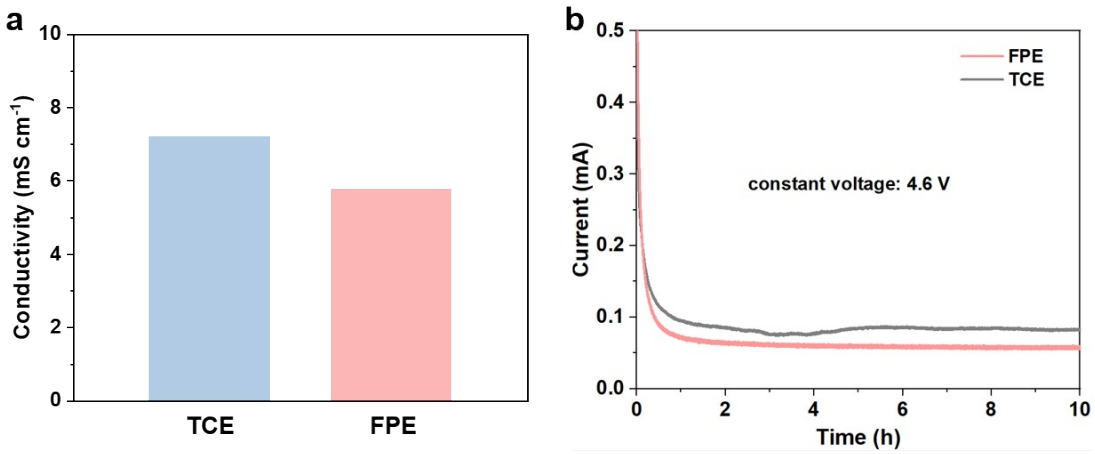

Fig. S3 (a) Ionic conductivities of TCE and FPE at room temperature (25 ℃). (b) Electrochemical floating analysis of FPE and TCE using LCO as cathode at a constant voltage of 4.6 V for 10 h.

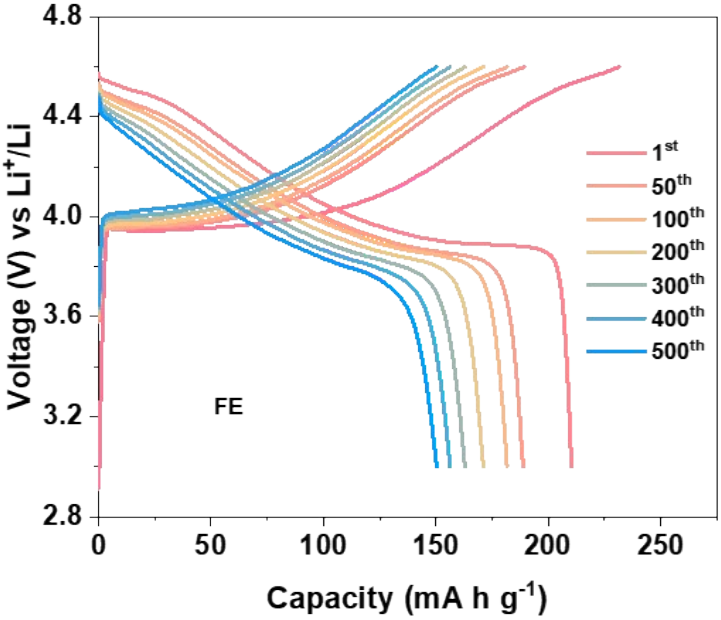

Fig. S4 GCD profiles of Li||LCO cells obtained in FE at 1 C at 3-4.6 V.

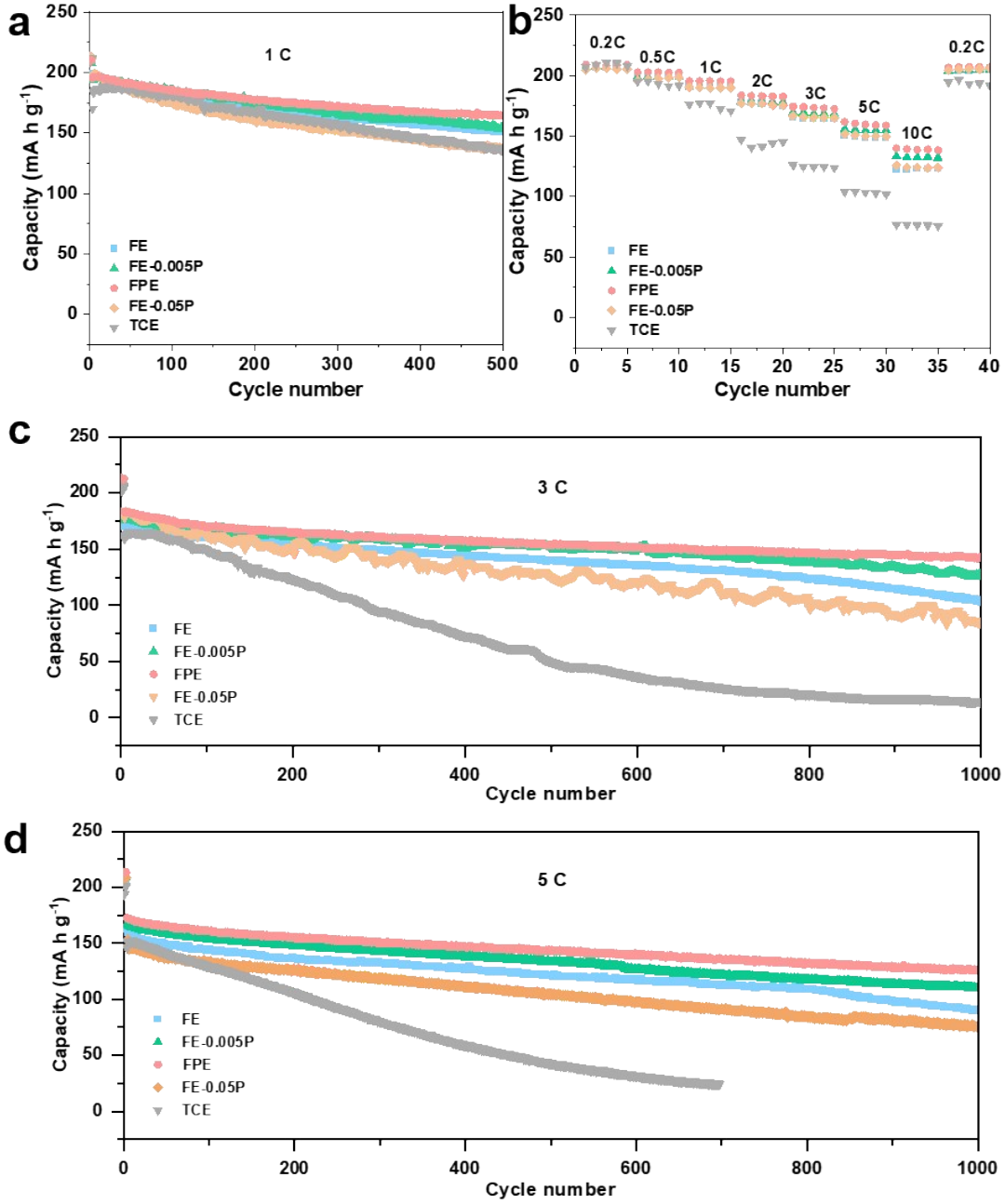

Fig. S5 Lithium storage performance of Li||LCO cells in TCE and the designed fluorine-based electrolytes with different $LiPO_2F_2$ contents at 3-4.6 V *vs.* Li^+/Li: (a) 1 C cycling stability, (b) rate performance, (c) fast charging/discharging performance at 3 C, and (d) superfast charging/discharging performance at 5 C.

Supplementary Note 1: Optimization of the content of $LiPO_2F_2$ additive

Considering the crucial role of additives for the formation of thin and robust electrode/electrolyte interface films, the content of additives was further optimized to obtain optimal electrochemical properties. As seen from Fig. S5, the cycling stability in FE was significantly improved compared with that in TCE at a current rate of 1 C when no $LiPO_2F_2$ was used. The reversible capacity and cycling stability increase continuously with the increase of $LiPO_2F_2$ content, which is attributed to the fact that this additive can promote the formation of a uniform and robust CEI film, effectively inhibiting transition metals dissolution and oxygen release under high voltage.[5] However, the cycling stability and reversible capacity retention decrease when the $LiPO_2F_2$ content is increased to 0.05 M, mainly caused by HF generated from $LiPO_2F_2$ attacking the cathode active materials. The optimal cyclability was achieved when $LiPO_2F_2$ content is 0.02 M, and 84.1% capacity retention is reached after 500 cycles with a reversible discharge capacity of 164 mA h g^{-1}.

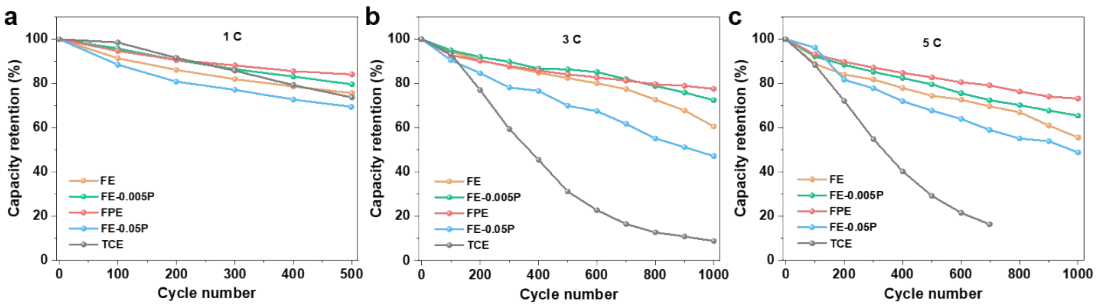

Fig. S6 The comparison of capacity retention for Li||LCO cells at (a) 1 C, (b) 3 C, and (c) 5 C in TCE and the designed fluorine-based electrolytes with different $LiPO_2F_2$ contents.

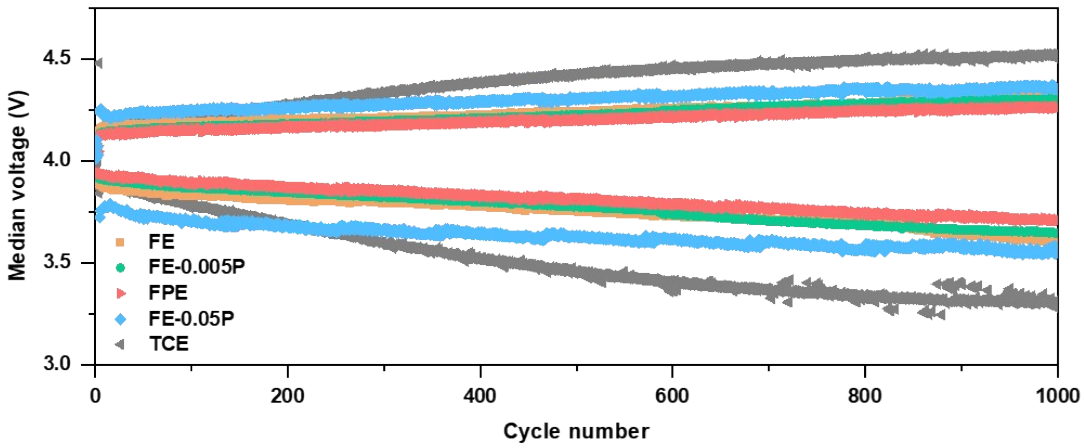

Fig. S7 Median charge/discharge voltages of Li||LCO cells at ultrahigh rate of 5 C in TCE and the designed fluorine-based electrolytes with different $LiPO_2F_2$ contents.

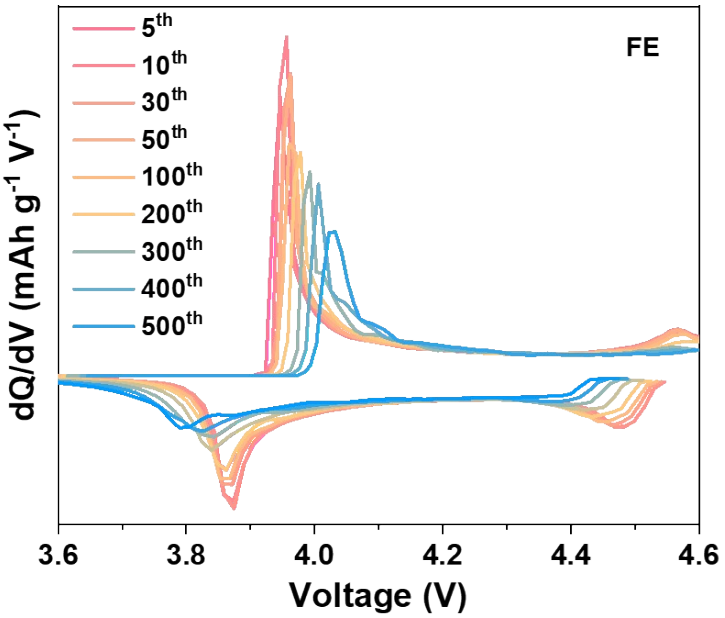

Fig. S8 The *d*Q/*d*V curves of Li||LCO cells at the selected cycles in FE at 3-4.6 V (*vs.* Li^+/Li).

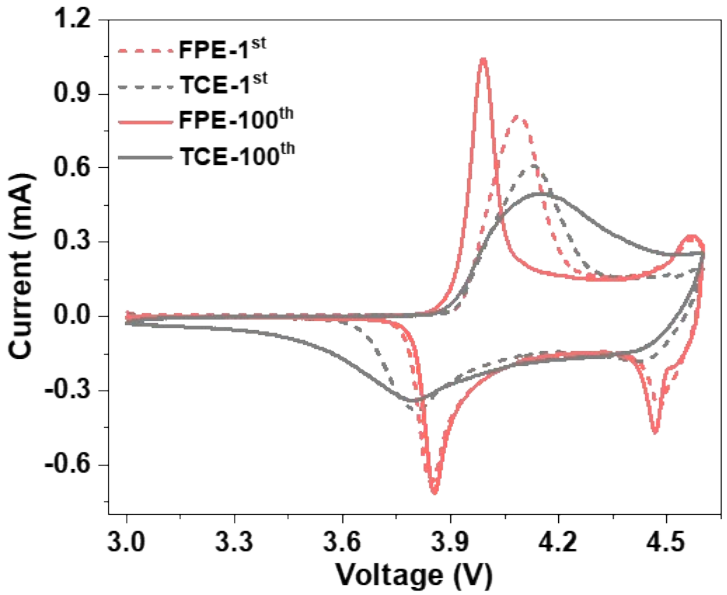

Fig. S9 CV curves of Li||LCO cells in two electrolytes of FPE and TCE at a scan rate of 0.1 mV s^{-1} at 3-4.6 V.

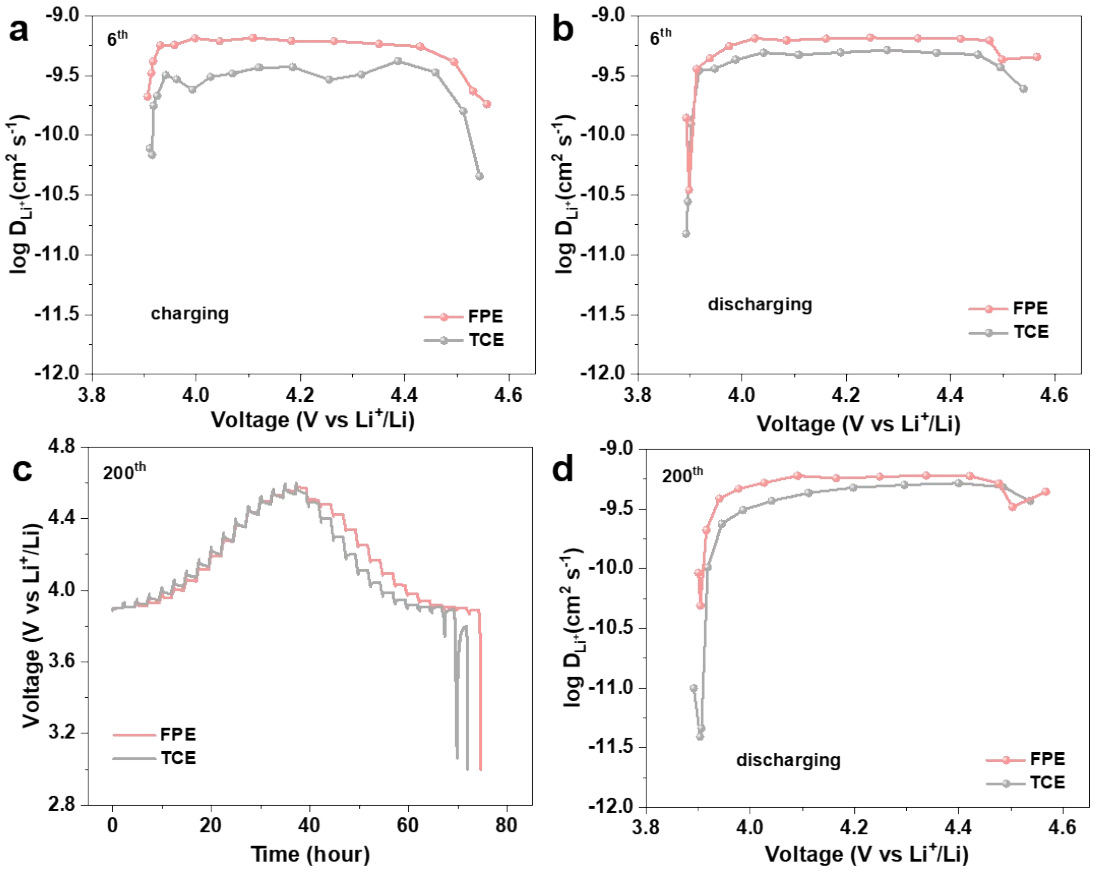

Fig. S10 The calculated lithium-ion diffusion coefficients according to the GITT profiles at the (a, b) 6th cycles. (c) The GITT profiles of LCO cathodes and (d) calculated lithium-ion diffusion coefficients according to GITT profiles at the 200th cycle in FPE and TCE.

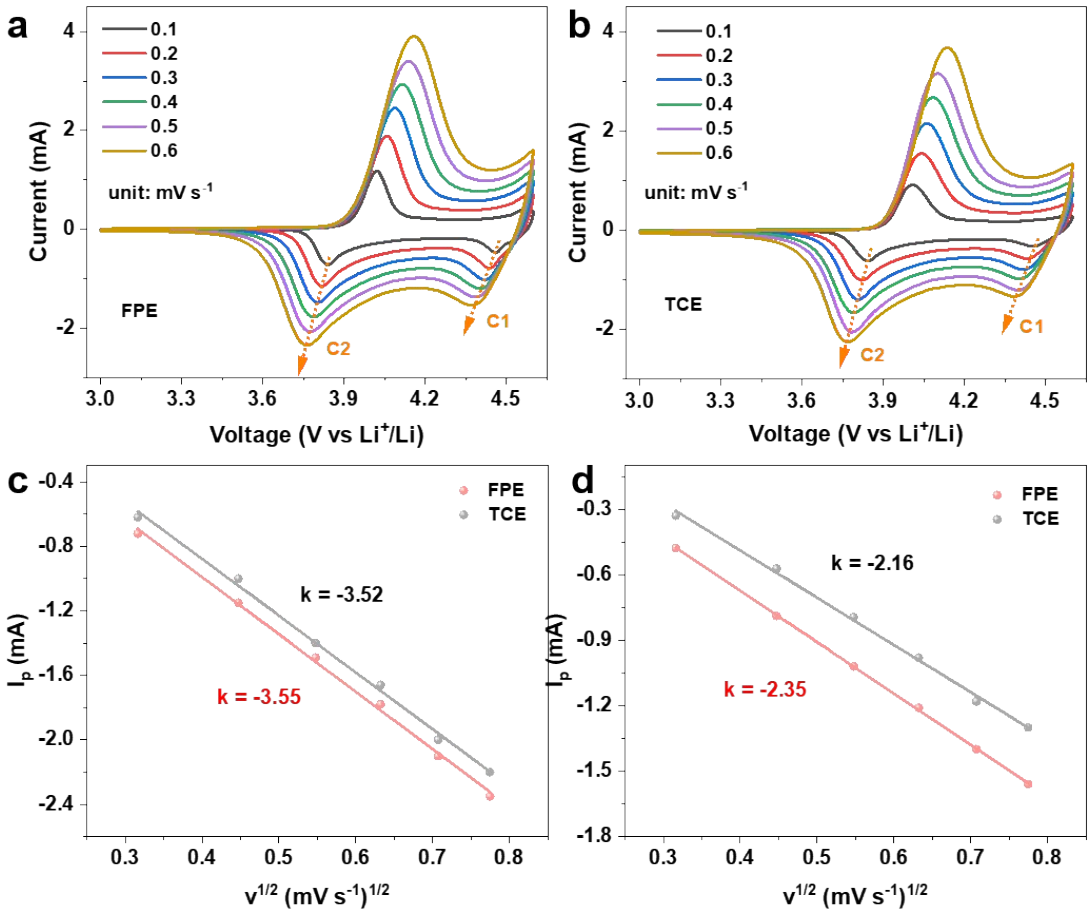

Fig. S11 CV measurements of LCO cathode in (a) FPE and (b) TCE at scan rates from 0.1 to 0.6 mV s^{-1} in the voltage range of 3.0-4.6 V (*vs.* Li^+/Li). Linear fitting for the (c) C_2 peak current and (d) C_1 peak current versus the square root of sweep speeds ($v^{1/2}$) collected from CV profiles.

Supplementary Note 2: Calculations of lithium-ion diffusion coefficient (D_{Li^+})

The D_{Li^+} is calculated from the following Equation:[6]

$$D_{Li+} = \frac{4}{\pi\tau}\left(\frac{n_m V_m}{S}\right)^2\left(\frac{\Delta E_S}{\Delta E_t}\right)^2\left(\tau \ll \frac{L^2}{D_{Li+}}\right)$$

where τ is the relaxation time, n_m is the molecular number of the LCO cathode, V_m is the molar volume of the cathode material, S is the surface area of LCO cathode, L is the thickness of the electrode, ΔE_s and ΔE_t are associated with the voltage change induced by the steady and the pulsed currents, respectively. As shown in Fig. 3d, and Fig. S10, the LCO in FPE all exhibits larger D_{Li^+} values both in the early cycles (6th cycle) and after the long cycles (200th cycle).

The D_{Li^+} of the LCO electrode can also be calculated through the CV method at different scanning speeds according to the Randles–Sevcik equation described as follows:[6]

$$i_p = 2.69 \times 10^5 n^{3/2} A D_{K+}^{1/2} v^{1/2} C$$

where i_p is the peak current, n is the transferring electron number during the redox reaction, A is the surface area of the LCO cathode, v is the scan rate, and C is the concentration of Li^+ in the LCO cathode. As presented in Fig. S11, a straight line is obtained by fitting i_p and $v^{1/2}$, and the slope of the straight line (k) is proportional to D_{Li^+}. The CV calculation results are in agreement with the results of GITT, that is, the LCO cathode in FPE shows faster Li^+ transport kinetics than that in TCE.

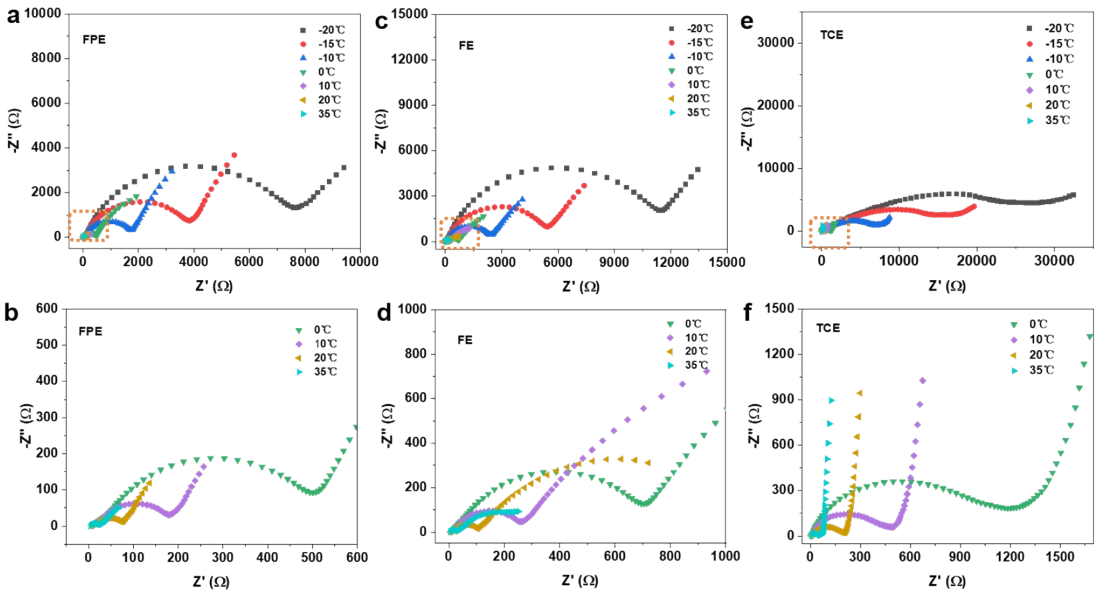

Fig. S12 EIS spectra of LCO cathodes in (a, b) FPE, (c, d) FE and (e, f) TCE at different temperatures at open circuit voltage.

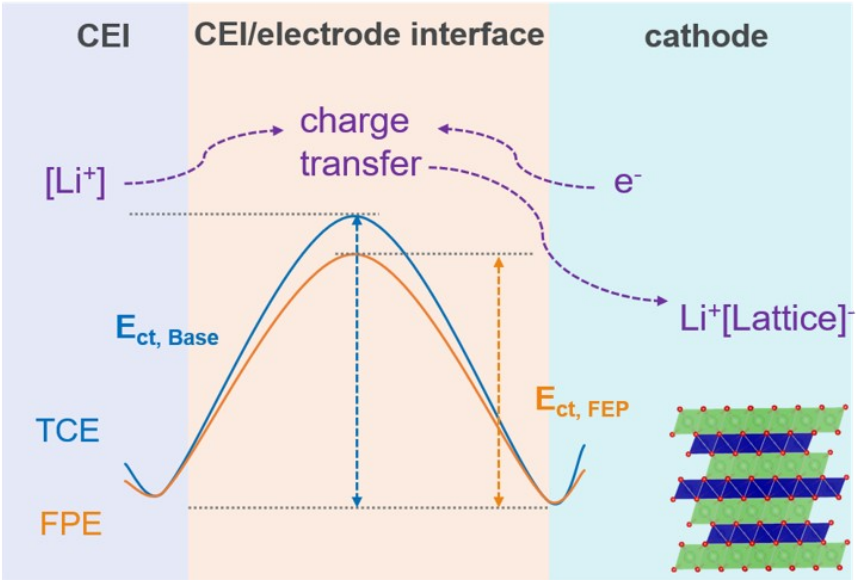

Fig. S13 Schematic of CEI compositions formed on LCO cathodes in two electrolytes of FPE and TCE, and the comparison of the charge transfer activation energy barriers.

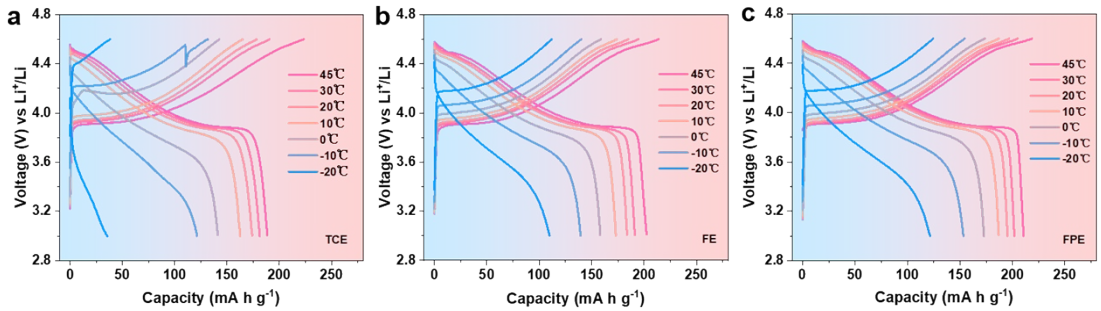

Fig. S14 GCD profiles of Li||LCO cells at 0.2 C in (a) TCE, (b) FE, and (c) FPE at 3-4.6 V at wide temperature.

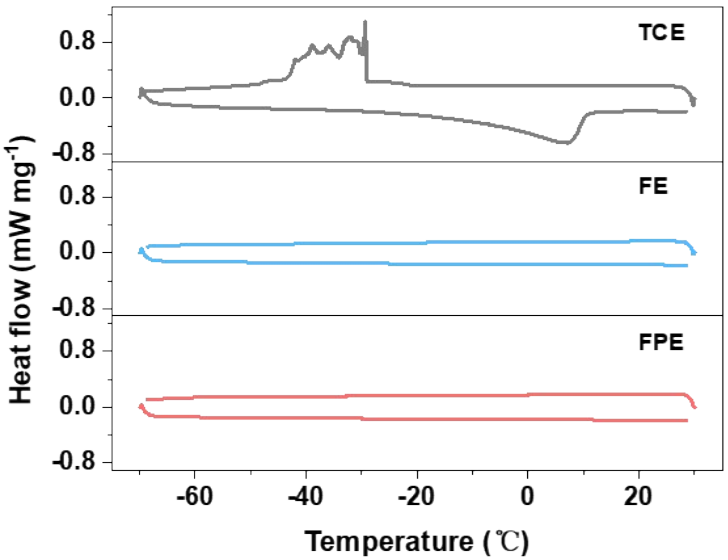

Fig. S15 DSC curves of TCE, FE, and FPE.

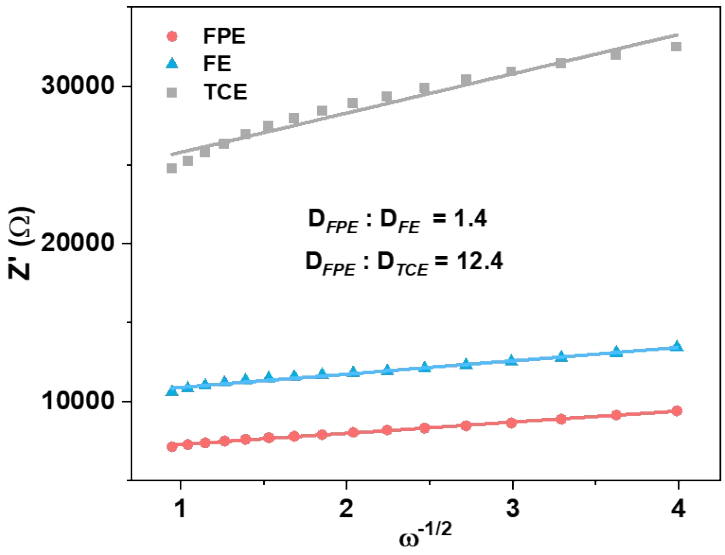

Fig. S16 Real parts of the complex impedance (Z′) versus square root of frequency ($\omega^{-1/2}$) of Li||LCO cells with FPE, FE, and TCE electrolytes at -20 ℃. The D_{Li}^{+} of the LCO electrode can also be calculated through the EIS method according to the relationship between the Z′ and square root of $\omega^{-1/2}$ in low frequency region in Fig. S12. The fitted line slop is corresponding to the Warburg coefficient (σ), and D_{Li}^{+} is proportional to $(1/\sigma)^2$.[7] Ultimately, the D_{Li}^{+} in FPE is calculated to be 1.4 and 12.4 times than those in FE and TCE, respectively.

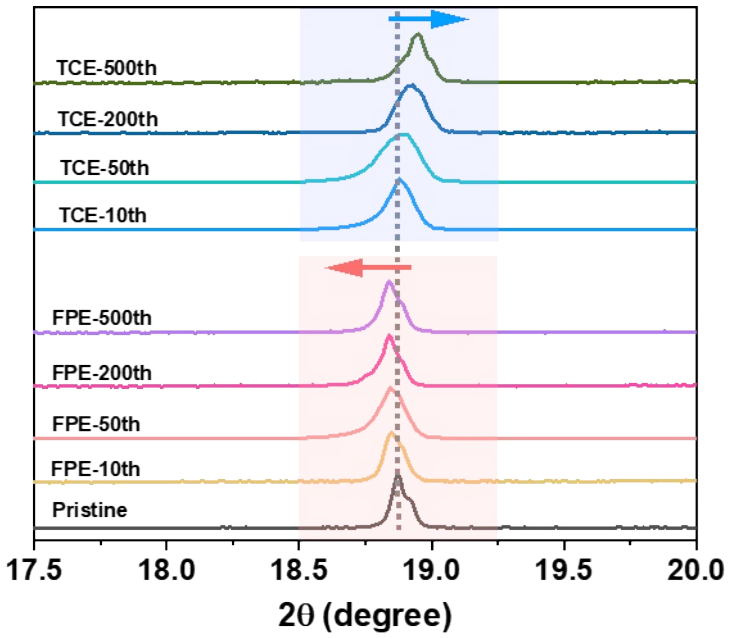

Fig. S17 XRD patterns of LCO cathodes in two electrolytes of FPE and TCE with different cycle numbers.

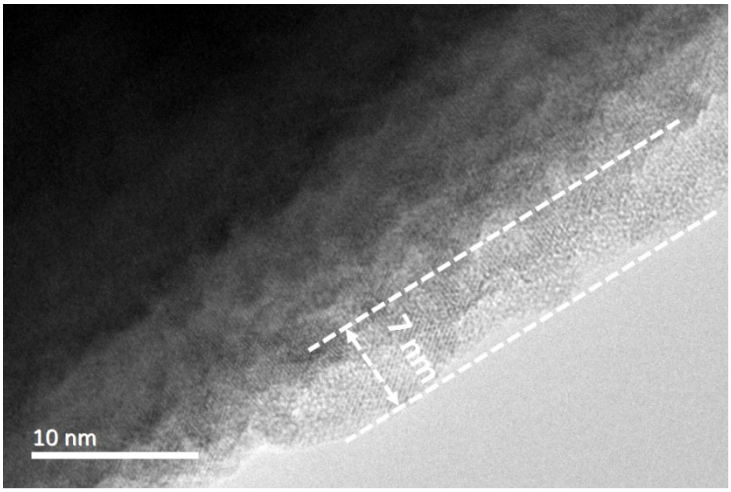

Fig. S18 HRTEM image of LCO cathode particles after 500 cycles in FE.

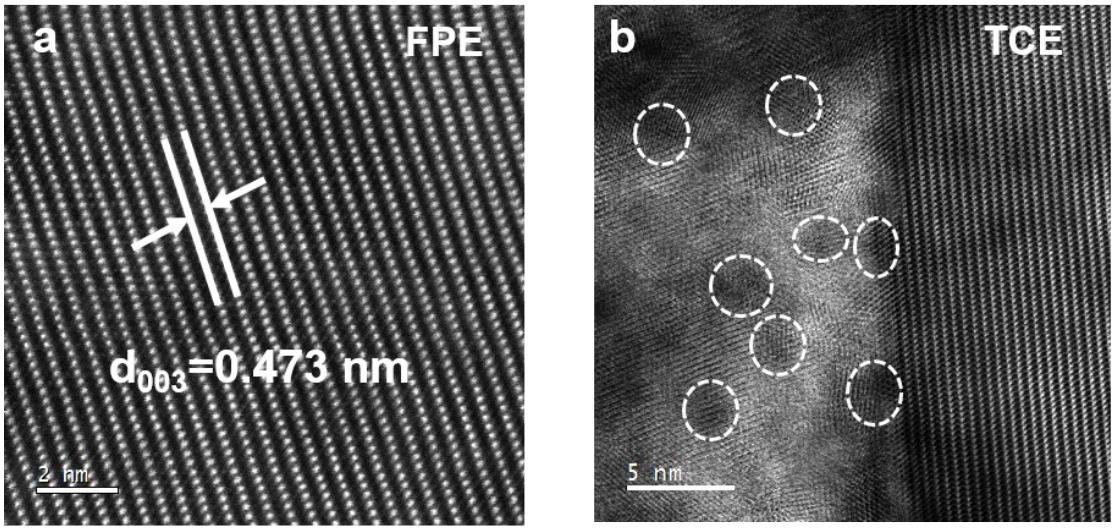

Fig. S19 High angle annular dark field scanning transmission electron microscope (HAADF-STEM) images of LCO cathode particles after 500 cycles in (a) FPE and (b) TCE.

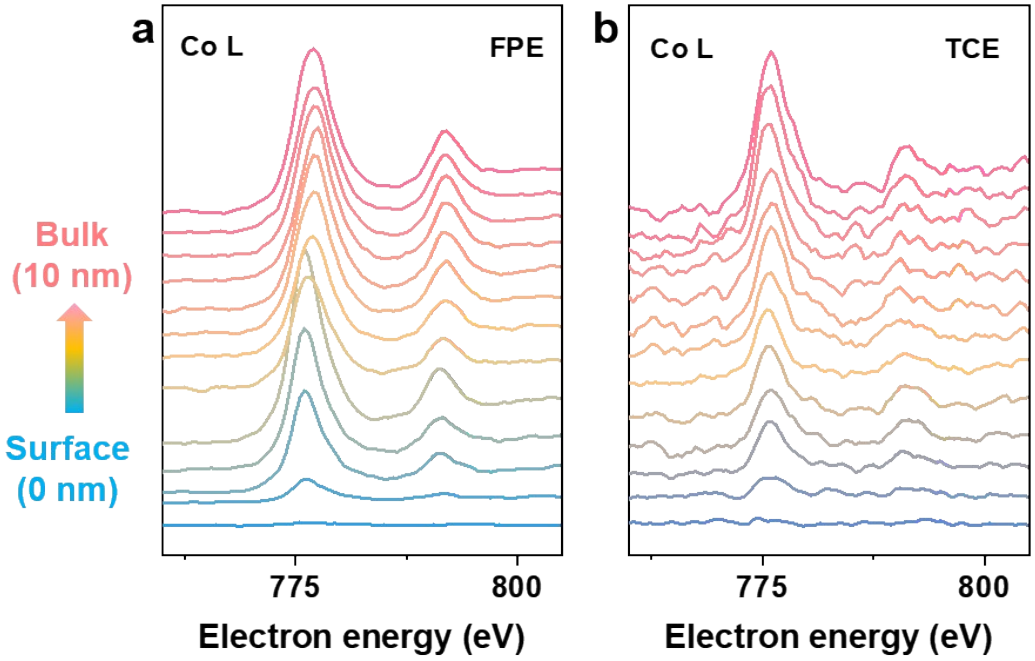

Fig. S20 EELS spectra of Co L-edge from the surface to the inner bulk of the cycled LCO cathodes in (a) FPE and (b) TCE.

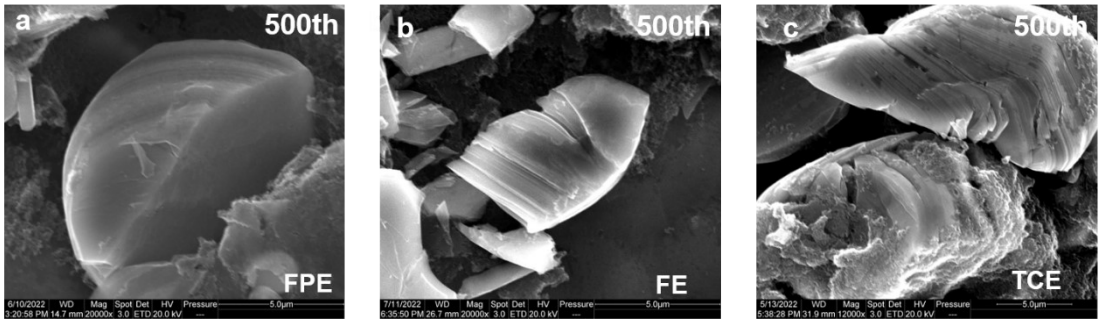

Fig. S21 SEM images of LCO particles in (a) FPE, (b) FE and (c) TCE after 500 cycles.

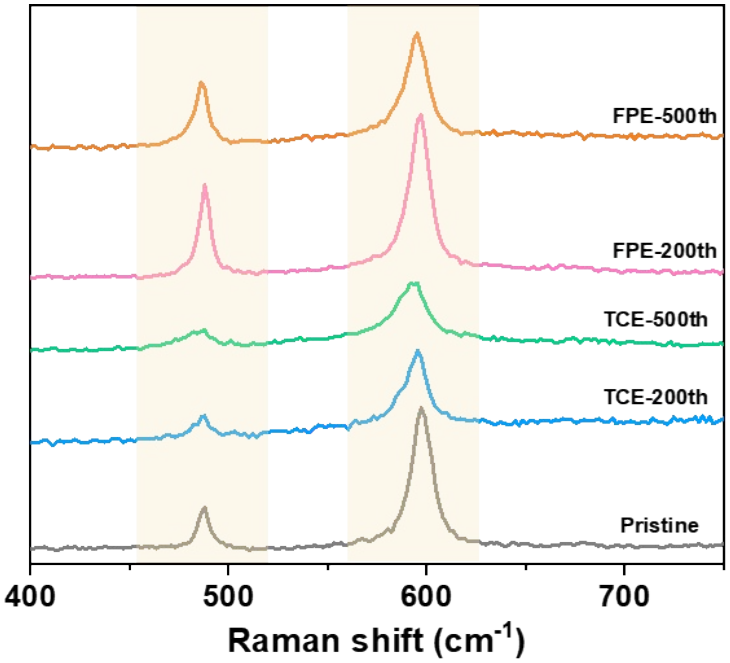

Fig. S22 Raman spectra of LCO cathodes in two electrolytes of FPE and TCE with different cycle numbers.

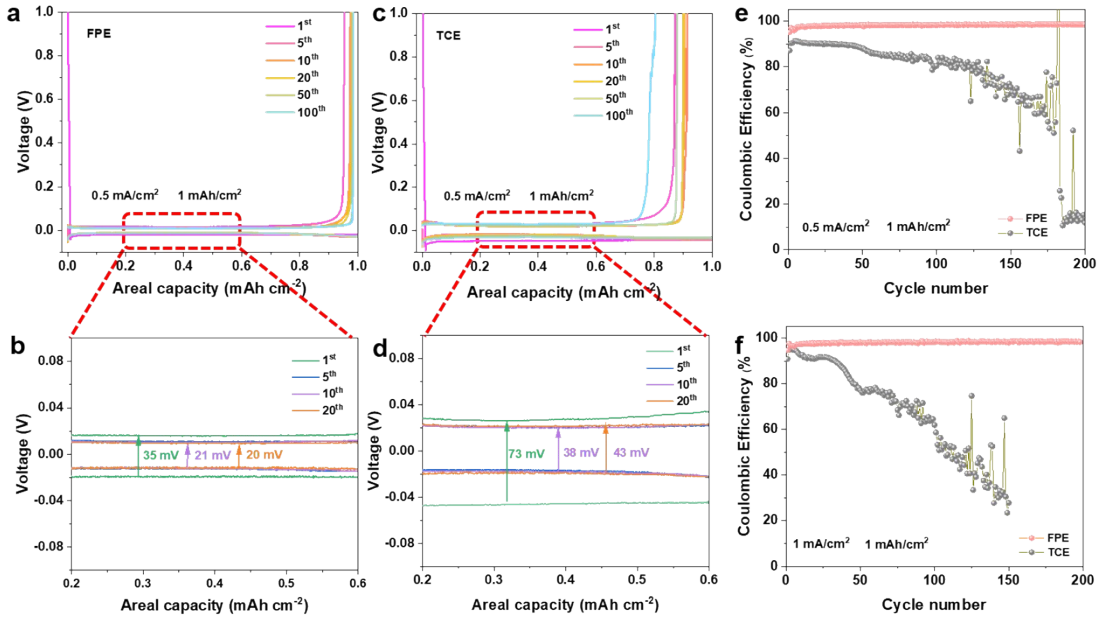

Fig. S23 Li deposition/stripping voltage profiles of selected cycles in (a, b) FPE and (c, d) TCE at 0.5 mA cm^{-2} in Li||Cu cells at a current density of 1 mA cm^{-2} in the range of 0-1 V. Coulombic efficiencies of Li deposition/stripping measured in Li||Cu cells in two electrolytes of FPE and TCE at current density of (e) 0.5 mA cm^{-2} and (f) 1 mA cm^{-2} in the range of 0-1 V.

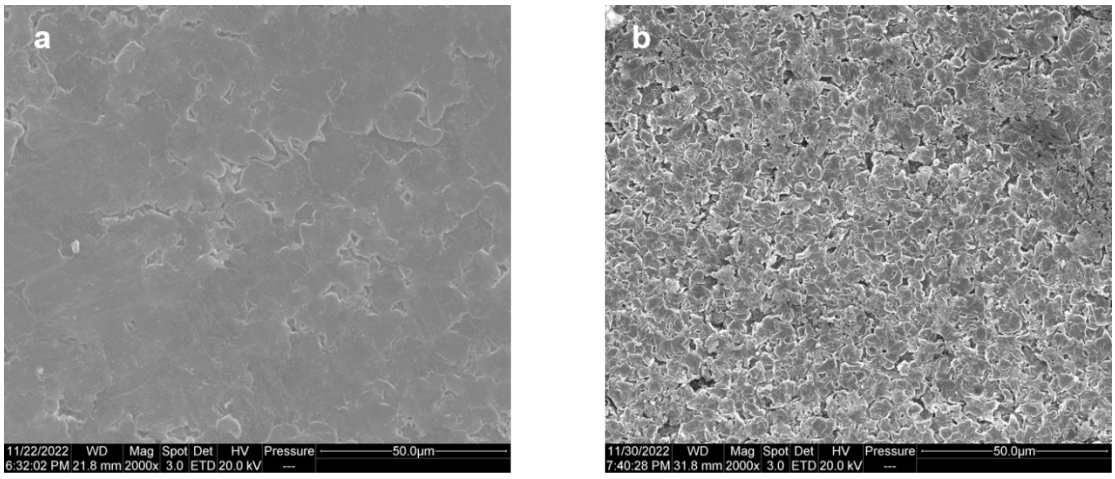

Fig. S24 SEM images of Li metals disassembled from Li||Cu cells after 100 cycles in (a) FPE (1 M $LiPF_6$ + 0.02 M $LiPO_2F_2$ in FEMC/DFEC/FEC/TTE (6:1:1:2 in vol)) and (b) 1 M $LiPF_6$ + 0.02 M $LiPO_2F_2$ in FEMC/DFEC/TTE (6:2:2 in vol).

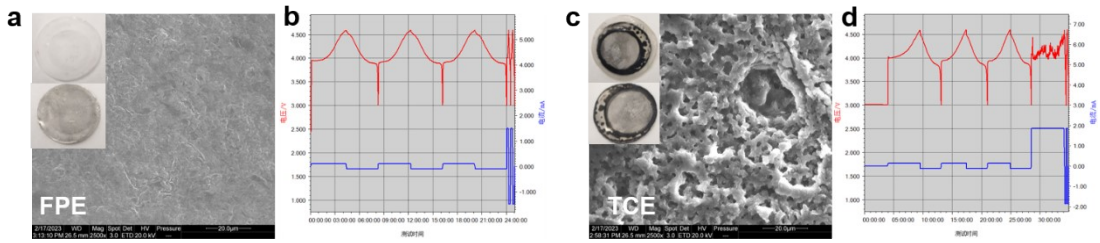

Fig. S25 SEM images of Li metals disassembled from Li||LCO cells after 3 cycles at 0.2 C and then 2 cycles at 3 C in (a) FPE and (c) TCE. Insets in (a, c) are the corresponding optical photos of Li anodes and diaphragms disassembled from Li||LCO cells in these two electrolytes. GCD profiles of Li||LCO cells in (b) FPE and (d) TCE at 0.2 C for 3 cycles and then 3 C for the following 2 cycles.

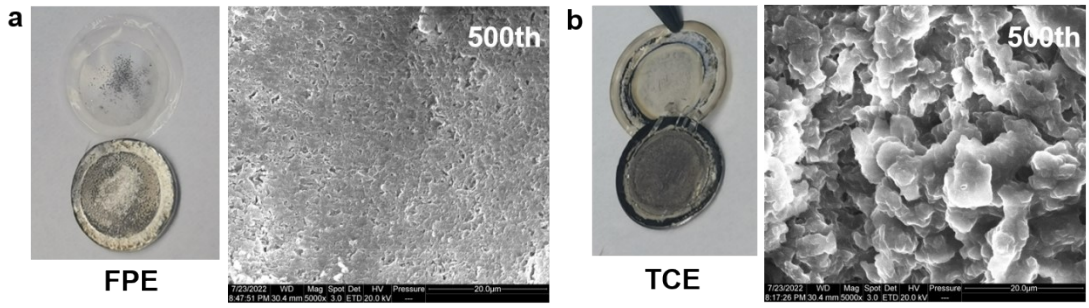

Fig. S26 Optical photographs and SEM images of Li metals disassembled from Li||LCO cells after 500 cycles at 3 C in (a) FPE and (b) TCE.

Supplementary Note 3: Compatibility of electrolyte with the Li anode

It has been reported that the high current densities would accelerate the evolution of Li dendrites and lead to the rapid formation of SEI with considerable resistance on Li anode surface.[8, 9] To analyze the effect of the fast-charging process on anodes, Li||LCO cells were disassembled when the current density was switched from 0.2 C to 3 C after 3 cycles at 0.2 C. As shown in Fig. S25, a large amount of dead Li was deposited on the separator in TCE, which could easily penetrate the separator and causes short circuit of batteries. This is caused by the typically sacrificial consumption of Li and serious parasitic reactions in carbonate-based electrolytes during the fast-charging process at high voltage. In contrast, the stable and low-impedance SEI film derived in FPE ensures the long-term cycling stability and fast-charging performance at high voltage. Li metals from Li||LCO cells after 500 cycles at high current density were also observed in Fig. S26. In TCE, some mossy-like dead lithium adhered to the separator, whereas the lithium remaining at anode was submicron-sized and unevenly distributed. While the surface of Li metal after cycling in FPE was very smooth, and there was almost no dead Li on the separator, indicating that the SEI layer was cooperatively stabilized, and the Li dendrites were effectively mitigated.

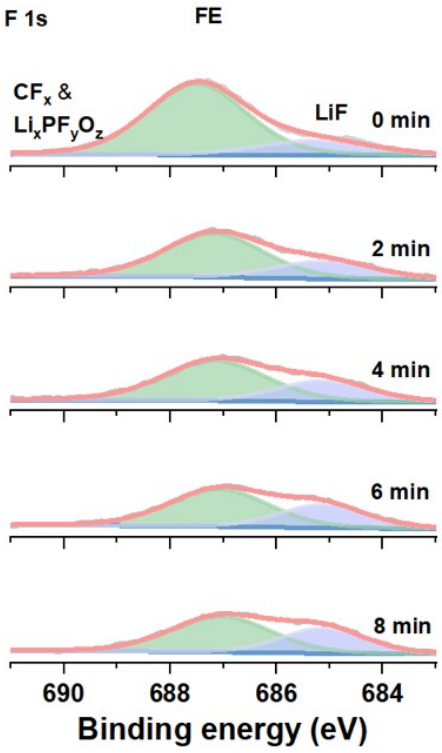

Fig. S27 XPS depth profiles of F 1 s of CEI formed on the surface of LCO in FE after 500 cycles.

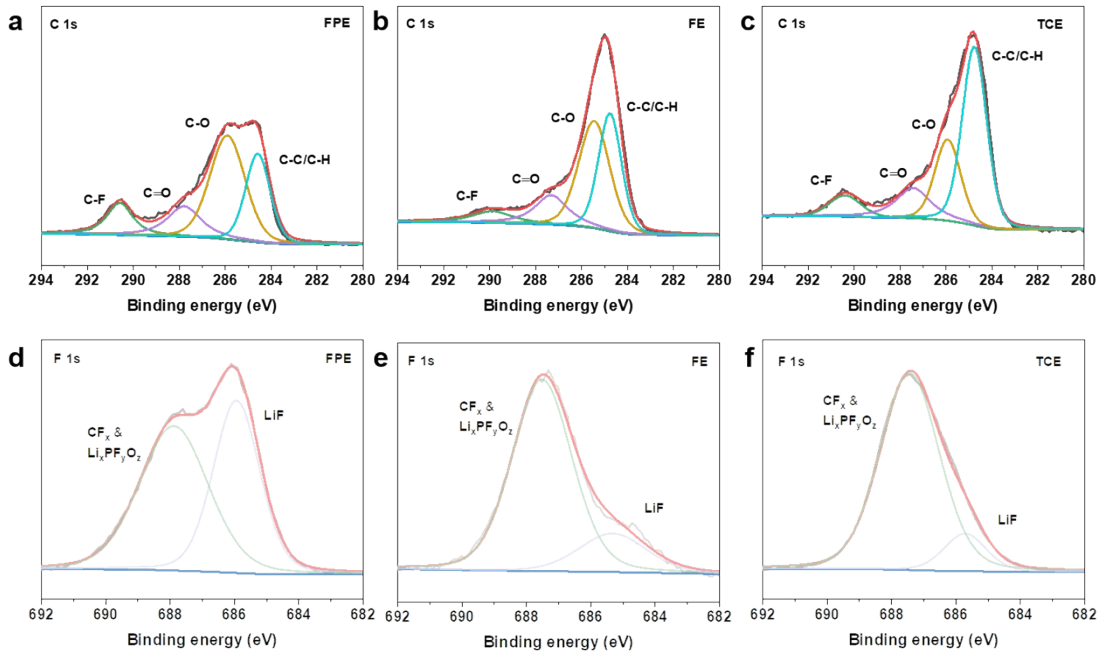

Fig. S28 C 1s spectra of CEI layers formed on the surface of LCO after 500 cycles in the (a) FPE, (b) FE, and (c) TCE electrolytes. F 1s spectra of CEI layers formed on the surface of LCO after 500 cycles in the (d) FPE, (e) FE, and (f) TCE electrolytes.

$$LiPF_6 + H_2O + nLi^+ - ne^- \rightarrow Li_xPO_yF_z + 2LiF + 2HF \quad (1)$$

$$PF_6^- + 2H_2O - e^- \rightarrow PO_yF_z^- + 4HF \quad (2)$$

$$PO_2F_2^- + 2H_2O + 4Li^+ \rightarrow Li_3PO_4 + LiF + HF + 3H^+ \quad (3)$$

Fig. S29 The decomposition mechanism of $LiPO_2F_2$-containing electrolyte.

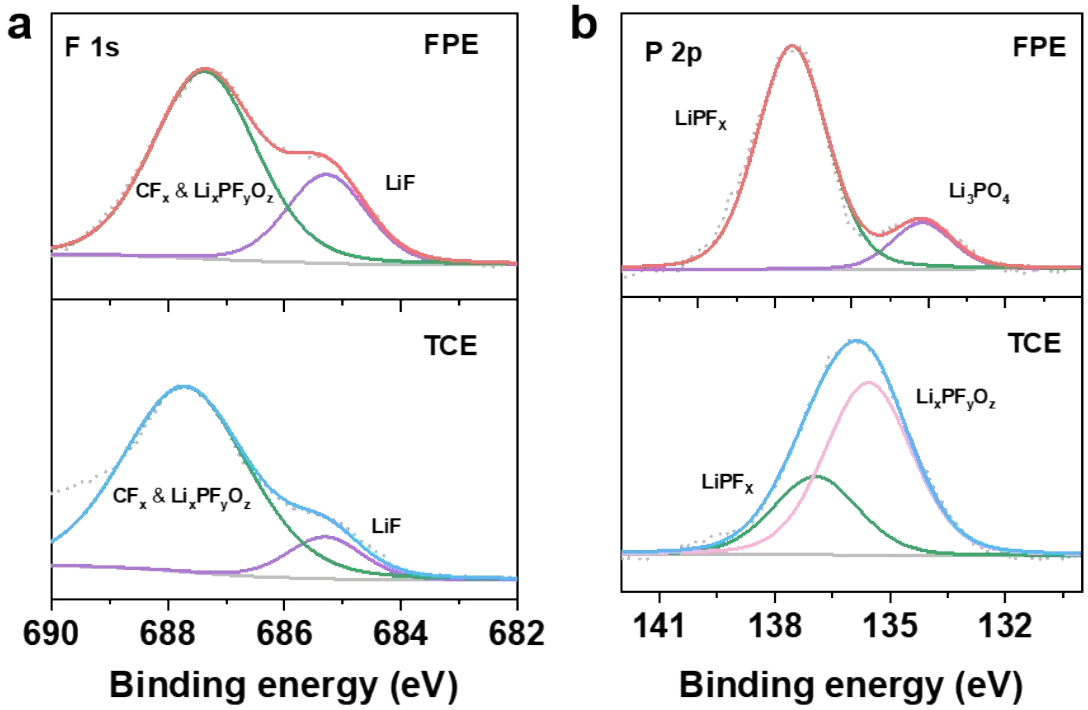

Fig. S30 (a) F 1s and (b) P 2p XPS spectra of SEI layers formed on the surface of Li anode after 4 cycles in two electrolytes of FPE and TCE.

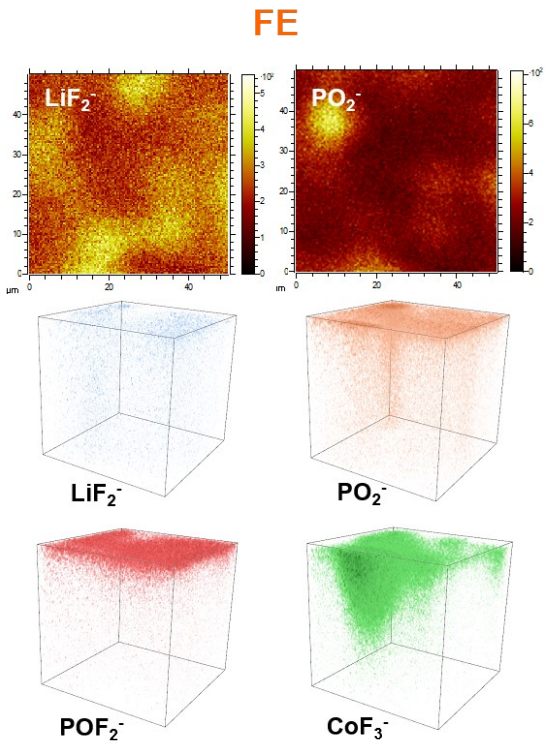

Fig. S31 TOF-SIMS 2D and 3D mapping images of several representative secondary ion fragments obtained from LCO cathode in FE after 500 cycles.

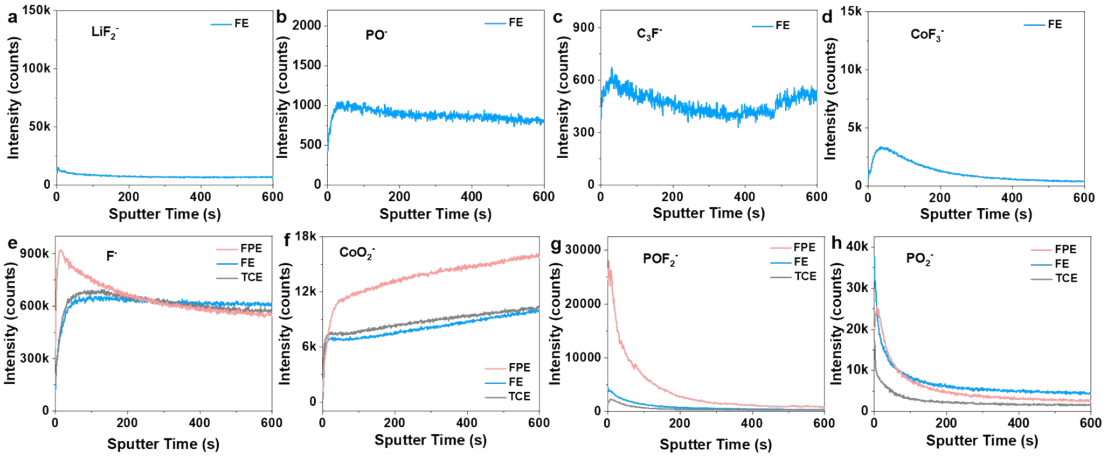

Fig. S32 TOF-SIMS depth profiles of (a) LiF_2^-, (b) PO^-, (c) C_3F^-, (d) CoF_3^-, (e) F^-, (f) CoO_2^-, (g) POF_2^-, and (h) PO_2^- species in CEI layer from LCO cathodes in the FPE, FE and TCE electrolytes after 500 cycles.

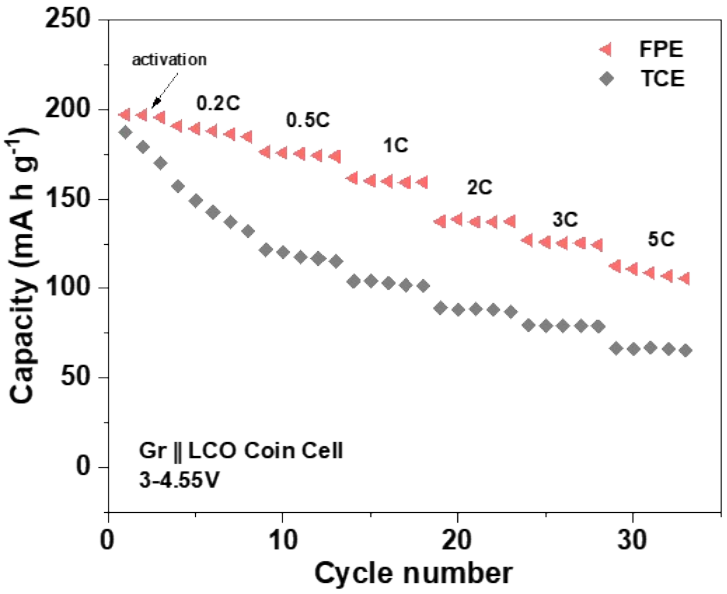

Fig. S33 Rate performance of Gr||LCO coin cells in the FPE and TCE at 3-4.55 V.

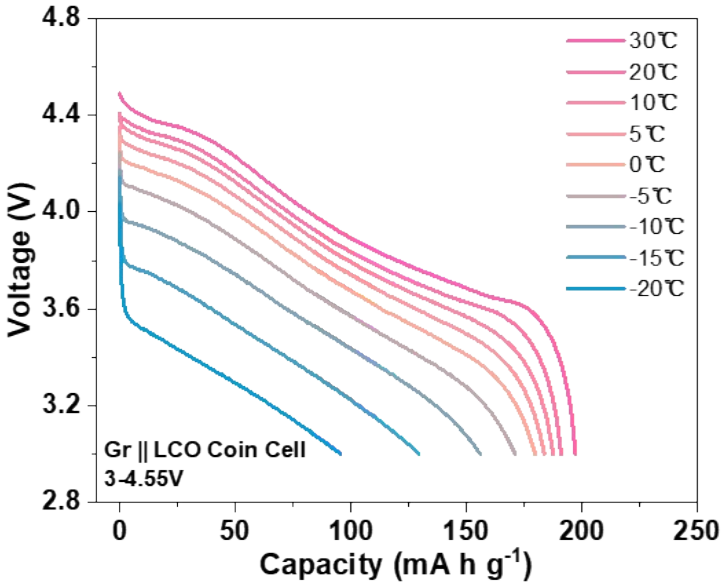

Fig. S34 Electrochemical performance of Gr||LCO coin cell in FPE at 3-4.55 V at wide temperature from −20 °C to 30 °C.

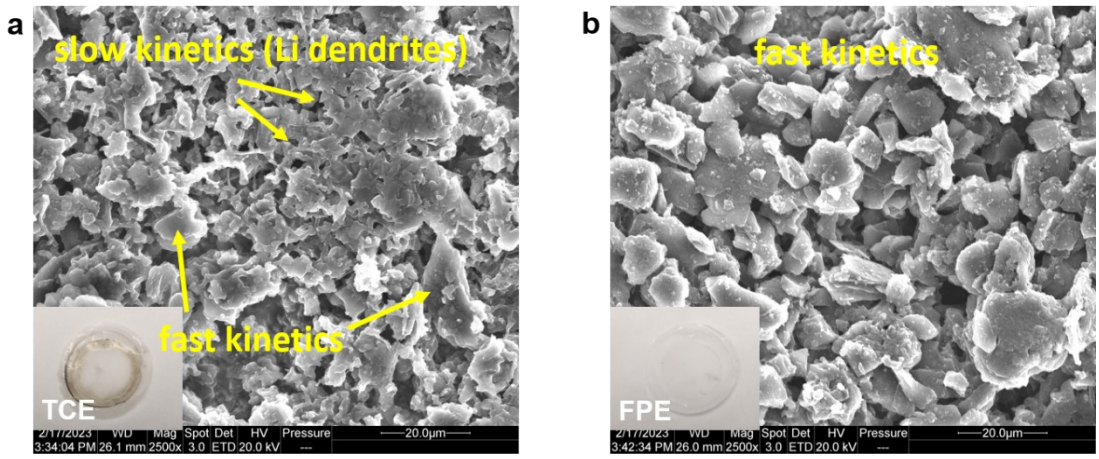

Fig. S35 Optical images of diaphragms (inset) and SEM images of graphite anodes from Gr||LCO coin cells in (a) TCE and (b) FPE after 4 cycles.

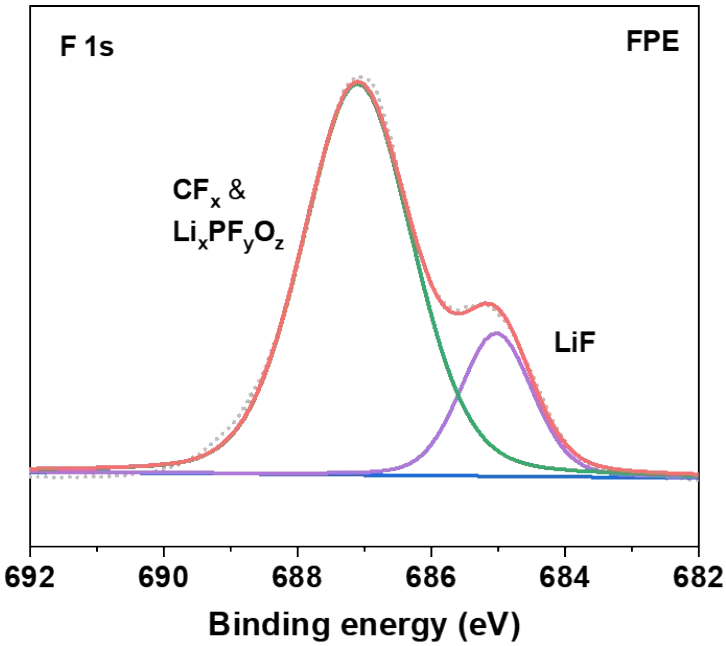

Fig. S36 F 1s XPS spectrum of SEI layers formed on the surface of graphite anode in Gr||LCO coin cells after 4 cycles in FPE.

Supplementary Note 4: Gr||LCO full coin cells

Besides the prolonged life span under fast charging conditions (Fig. 6b, c), the LiF- and Li_3PO_4-rich electrode/electrolyte interface is pivotal in enhancing the charge transport capability and rate performance of the Gr||LCO full cells. As illustrated in Fig. S33, the full cell exhibits more stable and enhanced capacities at various current densities from 0.2 C to 5 C in FPE. In addition, the wide-temperature electrochemical performance of the Gr||LCO full cells was also examined. The discharge capacity of Gr||LCO full cell in FEP was about 200 mA h g^{-1} at 30 °C, and it could still provide a high capacity of 96 mA h g^{-1} when at a reduced temperature of −20 °C (Fig. S34).

The morphologies of graphite anodes from Gr||LCO full cells after 4 cycles were analyzed, as exhibited in Fig. S35. Some micron-sized lithium dendrites adhered to the graphite particles in TCE, which is due to the precipitation of some Li metal on the surface of graphite anode restricted by dynamics when lithium ions are intercalated on graphite anode. The uneven Li metal layer not only causes serious safety hazards, but also aggravates the growth of SEI, which makes active lithium trapped into the dead lithium and cannot participate in the subsequent cycles, thereby resulting in severe capacity attenuation. In a stark contrast, the graphite electrode in FPE has almost no lithium metal precipitation, which is further verified by the clean separator. The interfacial chemistry of graphite anode was examined through XPS test, and a LiF-rich SEI layer was formed in FPE (Fig. S36). The kinetically matched fast interface phases are formed on both the cathode and the anode, ensuring outstanding fast-charging performance and high safety under high voltage.

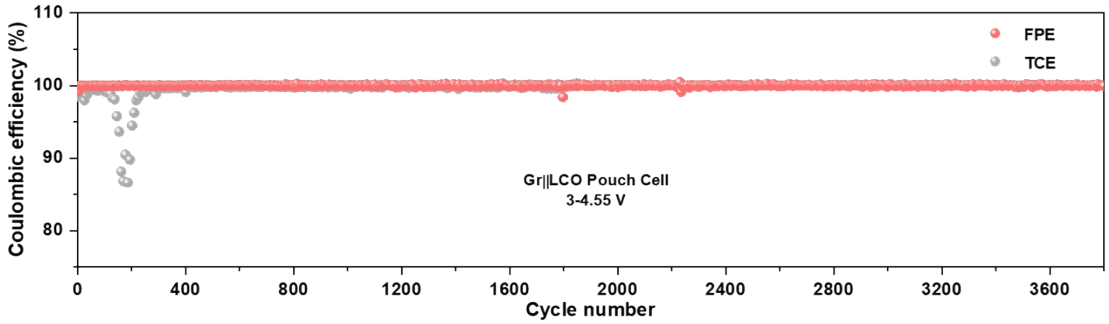

Fig. S37 Coulombic efficiencies of Gr||LCO pouch cells at 290 mA in two electrolytes of FPE and TCE at 3-4.55 V.

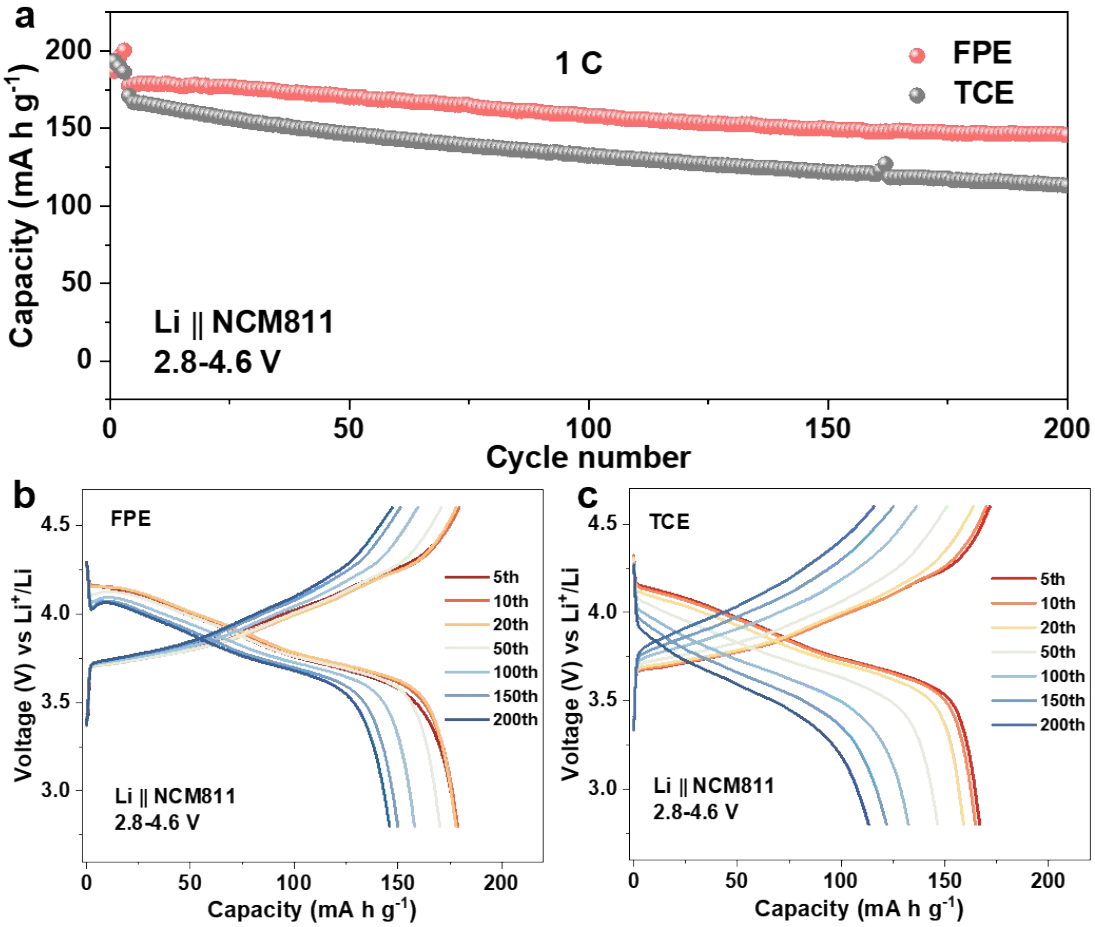

Fig. S38 (a) Cycling performance, and GCD profiles of Li||$LiNi_{0.8}Mn_{0.1}Co_{0.1}O_2$ (NCM811) cells in (b) FPE and (c) TCE measured at 1 C at 2.8-4.6 V.

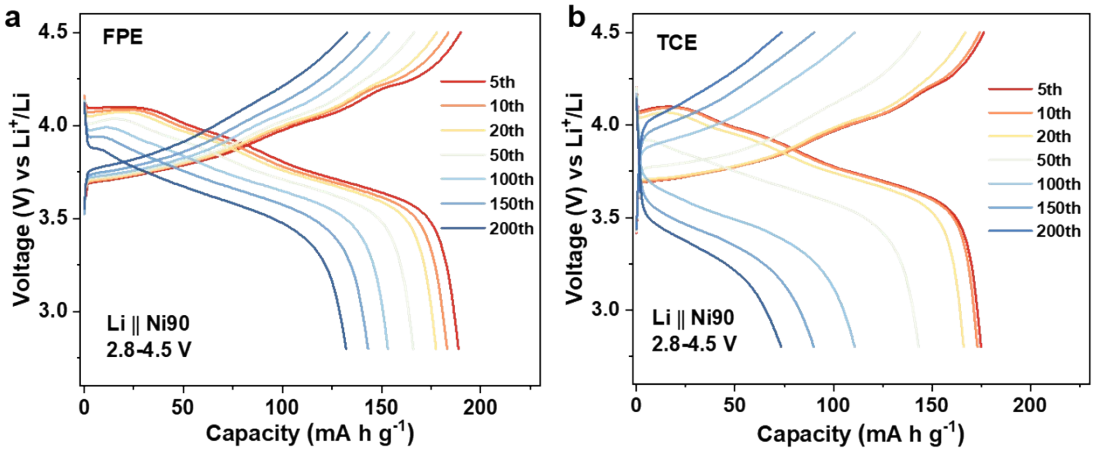

Fig. S39 GCD profiles of Li||$LiNi_{0.9}Mn_{0.05}Co_{0.05}O_2$ (Ni90) cells in (a) FPE and (b) TCE measured at 1 C at 2.8-4.5 V.

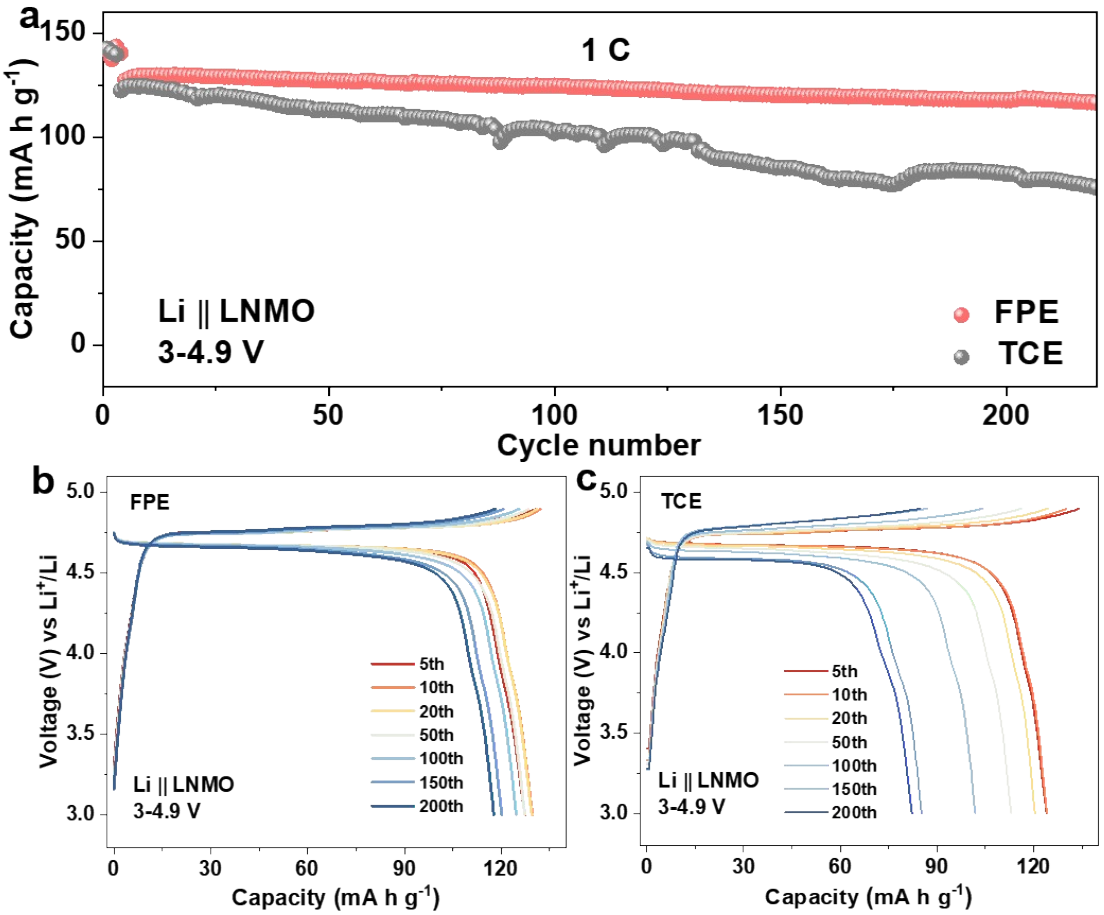

Fig. S40 (a) Cycling performance, and GCD profiles of Li||$LiNi_{0.5}Mn_{1.5}O_4$ (LNMO) cells obtained in (b) FPE and (c) TCE at 1 C at 3-4.9 V.

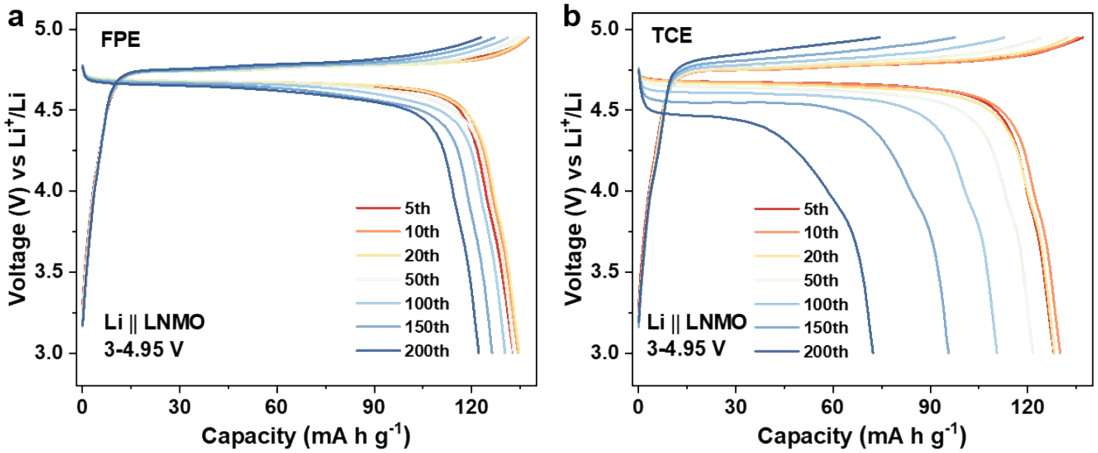

Fig. S41 GCD profiles of Li||LNMO cells in (a) FPE and (b) TCE at 1 C at 3-4.95 V.

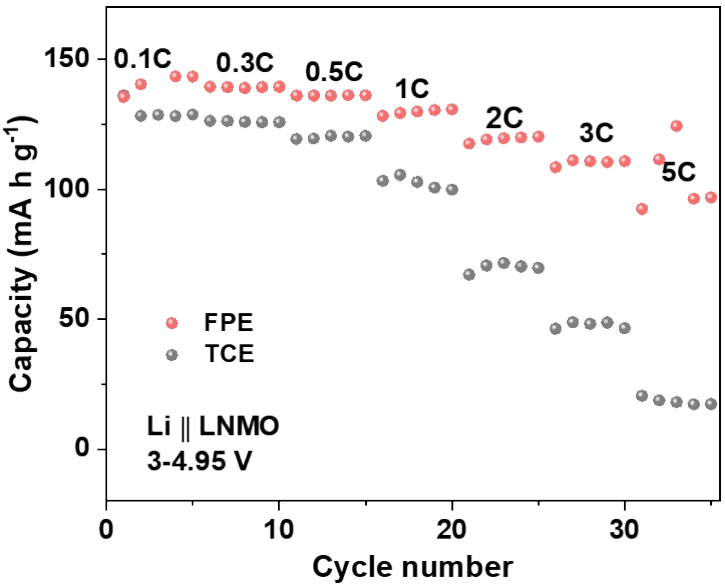

Fig. S42 Rate capability of Li||LNMO cells in two electrolytes of FPE and TCE at 3-4.95 V.

Supplementary Note 5: Generalization of electrolyte in Ni-rich and Co-free cathodes.

In addition to 4.6 V LCO cathode, high-voltage Ni-rich layered cathodes of $LiNi_{0.8}Mn_{0.1}Co_{0.1}O_2$ (NCM811) and $LiNi_{0.9}Mn_{0.05}Co_{0.05}O_2$ (Ni90) and Co-free $LiNi_{0.5}Mn_{1.5}O_4$ (LNMO) have also been applied to verify the generalization of our "cocktail strategy" electrolyte. As shown in Fig. S38, the cycling stability and selected GCD profiles of NCM811 cathode in FPE were examined in comparison with those in TCE. The reversible specific capacity reaches 150 mA h g^{-1} with a retention of 82% and no observable voltage decay after 200 cycles in FPE, which is higher than that in TE (only 113 mA h g^{-1}). Also, our electrolyte exhibits more stable voltage profiles and higher energy efficiency in Li||Ni90 cell, and the capacity of 132 mA h g^{-1} is obtained with a retention of 70%. In contrast, only 42% of the capacity remains in TCE (Fig. 6f and Fig. S39).

The application of FPE in high-voltage Co-free cathode was also evaluated. The capacity of 118 mA h g^{-1} is obtained with a retention of 93% and almost no voltage decay after 200 cycles in our electrolyte at the high charge cut-off voltage of 4.9 V. As a comparison, only 66% of the capacity remains in TCE electrolyte (Fig. S40). Furthermore, the Li||LNMO still exhibits extremely high electrochemical stability with a retention of 92% after 200 cycles when the charge cut-off voltage was improved to 4.95 V, which is much higher than 56% in TCE (Fig. 6g and Fig. S41). In addition, the Co-free cathode also offers superior rate performance in FPE, and high average capacities of 110 and 96 mA h g^{-1} can be delivered even at ultrahigh rates of 3 C and 5

C, respectively. In a sharp contrast, the LNMO in TCE displays a worse rate capability with capacities of only 48 and 18 mA h g^{-1} at 3 C and 5 C, respectively (Fig. S42).

Table S1 The initial charge-discharge specific capacities and Coulombic efficiencies of LCO cathodes in different electrolytes at 1 C.

Electrolyte	**FE**	**FE-0.005P**	**FPE**	**FE-0.05P**	**TCE**
1st-charge /mA h g^{-1}	231	230	231	240	260
1st-discharge /mA h g^{-1}	210	208	209	213	208
Coulombic efficiency	90.9%	90.4%	90.5%	88.7%	79.8%

Table S2 Performance comparison of our 4.6 V LCO in FPE and reported LCO batteries cycled in various advanced liquid electrolytes at a high cutoff voltage above 4.5 V.

Electrolytes	Electrodes	Voltage (V)	Current density	Capacity retention (cycle number)	Rate performance (mA h g^{-1})	Ref.
1 M $LiPF_6$ in FEMC/DFEC/FEC/TTE +$LiPO_2F_2$	**Li|LCO**	**3-4.6**	**a, 1 C; b, 5 C**	**a, 84.1% (500); b, 73.2% (1000)**	**140 (10 C)**	**This work**
1 M $LiPF_6$ in EC/DEC +SPTF	Li|LCO	3-4.65	1C/2C	88.2% (1000)	-----	10
1 M LiDFOB + 0.2 M $LiBF_4$ in FEC/DEC	Li|LCO	2.8-4.6	0.5 C	63.5% (400)	----	11
1 M $LiPF_6$ in EC/DMC + HDI + FEI + DPA	Li|LCO	3-4.6	0.5 C/1 C	74.7% (200)	132.5 (10 C, 3-4.5 V)	12
1 M $LiPF_6$ in FEC/FEMC/TTE + TMSB	Li|LCO	3-4.6	0.5 C	74.8% (300)	98 (10 C)	13
1 M $LiPF_6$ in EC/DEC + MMD	Li|LCO	3-4.6	a, 1 C; b, 1C/5C	a, 83.5% (200); b, 58.2% (1000)	132 (10 C)	2
1 M $LiPF_6$ in DMC/FEC/HFE + MSM	Li|LCO	2.75-4.55	1 C	74.9% (300)	130 (5 C)	14
1 M $LiPF_6$ in EC/DEC/EMC + LBTB	Li|LCO	3-4.4	1 C	73.21% (300)	164.4 (5 C)	15
1.3 M $LiPF_6$ in EC/EMC/DMC + $Mg(ClO_4)_2$	Li|LCO	3-4.55	150 mA g^{-1}	73% (100, 45°C)	------	16
2 M LiDFOB in EC/DMC	Gr|LCO	2.75-4.2	1 C	87% (800); 97% (160, 90°C)	-----	17
1 M LiFSI in $DMCF_3SA$	Li|LCO	a, 3-4.55 (13 mg cm^{-2}); b, 3-4.6 (11.0 mg cm^{-2})	150 mA g^{-1}	a, 89% (200); b, 85% (100)	183.1 (300 mA g^{-1})	18
1 M $LiPF_6$ in EC/DEC + KSeCN	Li|LCO	3-4.6	a, 1C; b, 2C/5C	a, 68.6% (750); b, 70.4% (1000)	198 (10 C)	10
1 M $LiPF_6$ in EC/EMC + FEC + HTCN	Li|LCO	3-4.6	a, 1C; b, 10 C	a, 75% (300); b, 73% (500)	137 (10 C)	19
1 M $LiPF_6$ in EC/DMC + $LiPO_2F_2$	Li|LCO	3-4.3	1 C	97.53% (160)	------	20
1 M $LiPF_6$ in EC/DEC + TFPB	Li|LCO	3-4.6	a, 1 C; b, 1C/5C	a, 84.6% (200); b, 63.3% (1000)	138 (10 C)	6
1.5 M $LiBF_4$ in DME/FEC	Li|LCO	3-4.6	0.5 C/1 C	55.5% (160)	138 (10 C)	21
1 M $LiPF_6$ in EC/DMC + FEC + 2-TP	Li|LCO	3-4.5	1 C	96% (200)	----	22
1.2 M $LiPF_6$-FEC/DMC/HFE + LiDFOB	Li|LCO	2.75-4.5 (8 mg cm^{-2})	200 mA g^{-1}	83.6% (300)	----	23
1 M $LiPF_6$ in EC/DEC + TAEC	Li|LCO	3-4.5	1 C	85.1% (100)	-----	24
1 M $LiPF_6$ in EC/DMC + TMB	Li|LCO	2.5-4.5	a, 0.1 C; b, 1 C	a, 81% (100); b, 82% (100)	110 (2 C)	25
1 M $LiPF_6$ in EC/EMC + PDTD	Li|LCO	3-4.6	1 C	60% (150)	-----	26

References

1. D. Wu, J. He, J. Liu, M. Wu, S. Qi, H. Wang, J. Huang, F. Li, D. Tang and J. Ma, *Adv. Energy Mater.*, 2022, **12**, 2200337.
2. Y. Zou, J. Zhang, J. Lin, D.-Y. Wu, Y. Yang and J. Zheng, *J. Power Sources*, 2022, **524**, 231049.
3. Z. Wang, H. Zhang, J. Xu, A. Pan, F. Zhang, L. Wang, R. Han, J. Hu, M. Liu and X. Wu, *Adv. Funct. Mater.*, 2022, **32**, 2112598.
4. Z. Wang, Y. Sun, Y. Mao, F. Zhang, L. Zheng, D. Fu, Y. Shen, J. Hu, H. Dong, J. Xu and X. Wu, *Energy Storage Mater.*, 2020, **30**, 228-237.
5. S. Tan, Z. Shadike, J. Li, X. Wang, Y. Yang, R. Lin, A. Cresce, J. Hu, A. Hunt, I. Waluyo, L. Ma, F. Monaco, P. Cloetens, J. Xiao, Y. Liu, X.-Q. Yang, K. Xu and E. Hu, *Nat. Energy*, 2022, **7**, 484-494.
6. Y. Zou, A. Fu, J. Zhang, T. Jiao, Y. Yang and J. Zheng, *ACS Sustainable Chem. Eng.*, 2021, **9**, 15042-15052.
7. J. Liu, B. Yuan, N. He, L. Dong, D. Chen, S. Zhong, Y. Ji, J. Han, C. Yang, Y. Liu and W. He, *Energy Environ. Sci.*, 2023, **16**, 1024-1034.
8. J. Xu, J. Zhang, T. P. Pollard, Q. Li, S. Tan, S. Hou, H. Wan, F. Chen, H. He, E. Hu, K. Xu, X.-Q. Yang, O. Borodin and C. Wang, *Nature*, 2023, **614**, 694-700.
9. S. S. Zhang, *InfoMat*, 2021, **3**, 125-130.
10. Y. Yan, S. Weng, A. Fu, H. Zhang, J. Chen, Q. Zheng, B. Zhang, S. Zhou, H. Yan, C.-W. Wang, Y. Tang, H. Luo, B.-W. Mao, J. Zheng, X. Wang, Y. Qiao, Y. Yang and S.-G. Sun, *ACS Energy Lett.*, 2022, **7**, 2677-2684.
11. P. Bai, X. Ji, J. Zhang, W. Zhang, S. Hou, H. Su, M. Li, T. Deng, L. Cao, S. Liu, X. He, Y. Xu and C. Wang, *Angew. Chem. Int. Edit.*, 2022, **61**, 202202731.
12. Y. Qin, K. Xu, Q. Wang, M. Ge, T. Cheng, M. Liu, H. Cheng, Y. Hu, C. Shen, D. Wang, Y. Liu and B. Guo, *Nano Energy*, 2022, **96**, 107082.
13. J. Zhang, P.-F. Wang, P. Bai, H. Wan, S. Liu, S. Hou, X. Pu, J. Xia, W. Zhang, Z. Wang, B. Nan, X. Zhang, J. Xu and C. Wang, *Adv. Mater.*, 2022, **34**, 2108353.
14. X. Kong, R. Zhou, J. Wang and J. Zhao, *ACS Appl. Energy Mater.*, 2019, **2**, 4683-4691.
15. Z. Sun, H. Zhou, X. Luo, Y. Che, W. Li and M. Xu, *J. Power Sources*, 2021, **503**, 230033.
16. J. Lim, A. Choi, H. Kim, S. W. Doo, Y. Park and K. T. Lee, *J. Power Sources*, 2019, **426**, 162-168.
17. J.-N. Zhang, Q. Li, C. Ouyang, X. Yu, M. Ge, X. Huang, E. Hu, C. Ma, S. Li, R. Xiao, W. Yang, Y. Chu, Y. Liu, H. Yu, X.-Q. Yang, X. Huang, L. Chen and H. Li, *Nat. Energy*, 2019, **4**, 594-603.
18. W. Xue, R. Gao, Z. Shi, X. Xiao, W. Zhang, Y. Zhang, Y. G. Zhu, I. Waluyo, Y. Li, M. R. Hill, Z. Zhu, S. Li, O. Kuznetsov, Y. Zhang, W.-K. Lee, A. Hunt, A. Harutyunyan, Y. Shao-Horn, J. A. Johnson and J. Li, *Enery. Environ. Sci.*, 2021, **14**, 6030-6040.
19. X. Yang, M. Lin, G. Zheng, J. Wu, X. Wang, F. Ren, W. Zhang, Y. Liao, W. Zhao, Z. Zhang, N. Xu, W. Yang and Y. Yang, *Adv. Funct. Mater.*, 2020, **30**, 2004664.
20. G. Yang, J. Shi, C. Shen, S. Wang, L. Xia, H. Hu, H. Luo, Y. Xia and Z. Liu, *RSC Adv.*, 2017, **7**, 26052-26059.
21. Z. Jiang, J. Mo, C. Li, H.-W. Li, Q. Zhang, Z. Zeng, J. Xie and Y. Li, *Energy Environ. Mater.*, 2022, **6**, 12440.

22. X. Wen, M. Chen, X. Zhou, S. Chen, H. Huang, J. Chen, D. Ruan, W. Xiang, G. Zhang and W. Li, *J. Phys. Chem. C*, 2022, **126**, 282-295.
23. S. Lin and J. Zhao, *ACS Appl. Mater. Interfaces*, 2020, **12**, 8316-8323.
24. Y. Zheng, W. Fang, H. Zheng, Y. Su, X. Liang, C. Chen and H. Xiang, *J. Electrochem. Soc.*, 2019, **166**, A3222.
25. Q. Liu, G. Yang, S. Liu, M. Han, Z. Wang and L. Chen, *ACS Appl. Mater. Interfaces*, 2019, **11**, 17435-17443.
26. S. Wu, Y. Lin, L. Xing, G. Sun, H. Zhou, K. Xu, W. Fan, L. Yu and W. Li, *ACS Appl. Mater. Interfaces*, 2019, **11**, 17940-17951.